On modelling of consolidation processes in geological materials

Abstract

Low-permeablity materials may be seen as natural geological barriers for radioactive waste repositories. However, to ensure their safe performance, a good understanding of their mechanical properties is required. Although the standard Biot's poroelastic model is widely used to estimate the key properties of these materials, experimental observations differ from this mathematical formulation and suggest that a more complex rock deformation behaviour to include a creep effect is needed. In this study, the Biot's differential equations are modified to include a rheological skeleton. In comparison with other existing models, here we propose a formulation with a minimal parametric uncertainty: we show that with just one additional physically-based parameter, the experimental creep behaviour is properly described. This enhanced model is implemented within a finite element framework and employed in a fitting algorithm to extract the hydro-mechanical properties from experimental data. To illustrate its generality, we analyse laboratory tests performed on three different types of materials: (a) an unlithified lower Oligocene clay from Belgium (Boom Clay), (b) an indurated Jurassic mudrock (Callovo-Oxfordian mudstone) and (c) a Triassic siltstone (Mercia Mudstone Formation). Numerical fits to the data support the validity of this approach and demonstrate its applicability to a range of low-permeability materials regardless of mineralogy or burial history.

Keywords: consolidation tests, Biot's model, elasticity, viscosity, creep, porous medium

1. Introduction

Diagenetic processes occurring during burial will have a profound effect on the hydro-mechanical (HM) behaviour of mudrocks (Horseman and Harrington, 1996). However, the properties of a mudrock are not solely governed by diagenesis alone and a number of processes occurring before, during and after can play an important role in defining the structural characteristics of such materials. Most important of these is the role of stress history, which can be affected as a direct result of both tectonic and erosional forces combining to produce deformation, uplift and exhumation. The importance of these processes and their impact on the HM behaviour of mudrocks can be profound (Bjerrum, 1967; Skempton, 1970 and Novello, 1987). In a geological repository for radioactive waste, the ability to predict long-term changes in rock properties over protracted periods of time is a central requirement in the development of any safety case. In many geological disposal concepts, clay-based formations are considered favourable options for the hosting of such underground repositories. Thus, understanding changes in HM behaviour as a repository undergoes either burial or exhumation is fundamental to the long-term prediction of both natural and engineered barriers. Central to this understanding is an ability to quantitatively model these processes in order to test material sensitivities, validate repository concepts and allow scenario analyses to be undertaken. With this in mind, laboratory experiments measuring the consolidation (loading) and rebound (unloading) of rock samples are undertaken to provide essential data with which to test and validate HM models.

Experiments on sediments and sedimentary rocks have shown that additional volume strain can accumulate, even after the sediment is fully consolidated to the applied stress (Atkinson and Bransby, 1978). Bishop and Lovebury (1969) demonstrated that remoulded London clay still showed creep three years after primary consolidation was complete. The mechanisms of secondary consolidation possibly include: (i) grain surface diffusion, (ii) time-dependent crack generation associated with a redistribution of stored strain energy and (iii) diffusion in microfractures, with stress corrosion weakening the fracture tips. Thus, this creep behaviour should be considered in the mathematical formulation designed to extract the hydro-mechanical properties from experimental data.

The analysis of the consolidation of soil media was first addressed in a one-dimensional setting by Terzaghi (1925) and was later generalized by Biot (1941). Since these first contributions, where soil was described as an ideal linear elastic material, significant progress has been made to account for more realistic deformation behaviours. In these enhanced models, the standard Biot's consolidation theory is usually modified to account for, among others, viscoelastic, elasto-plastic, elasto-viscoplastic or damage soil skeletons. As contributions in this direction, and without attempting to be complete, we refer to the models proposed by Oka et al. (1986), Bardet (1992), Manoharan and Dasgupta (1995), Fowler and Noon (1999), Hamiel et al. (2004) and references therein.

These extended mathematical models led to a more appropriate characterisation of the consolidation of porous media. Nevertheless, their main disadvantage arises from the requirement of additional parameters for both the solid skeleton and the fluid. Determination from experimental data in low and ultra-low permeability materials can be challenging or even unfeasible and hence, simple models such as the standard Biot's consolidation theory are still preferred when characterising materials for real-life applications.

In this paper, a viscoelastic model with a minimal parametric uncertainty is proposed. In this contribution, the standard Biot's poroelastic model (Section 3) is modified to include the creep effect observed in experimental tests (Section 4). In contrast to some other techniques, only one additional parameter with respect to the classical Biot's model is needed. The simplicity of this approach and the clear physical meaning of the three parameters involved is used here to derive an algorithm for parameter identification, which successfully performs with experimental data obtained from consolidation experiments conducted on different kinds of clay-based materials (Section 5).

2. Experimental set-up and test methodology

Testing was undertaken using a BGS custom-designed isotropic permeameter consisting of five main components: (1) a specimen assembly, (2) a 70 MPa rated pressure vessel and associated confining pressure system, (3) a fluid injection system, (4) a backpressure system, and (5) a National Instruments data acquisition system. Each specimen was sandwiched between two stainless steel end-caps and jacketed in heat-shrink Teflon to exclude confining fluid and provide a flexible pressure seal. A unique 'lock-ring' arrangement (Figure 1) was then placed over the jacketed specimen, so as to provide a leak-tight seal. The inlet and outlet zones for permeant flow through the specimen were provided by porous filter discs mounted between the sample and the load bearing surface of the end-caps. Once complete the sample assembly was then inserted into the pressure vessel and an isotropic stress applied using water.

Volumetric flow rates were controlled or monitored using a pair of syringe pumps operated from a single digital control unit. Each pump can operate in either a constant pressure or constant flow mode. A programme written in LabVIEWTM elicited data from each pump at pre-set time intervals. Testing was performed in an air-conditioned laboratory at a nominal temperature of 20 °C. All pressure sensors were calibrated against laboratory standards.

Analysis in this paper relates to data from experiments conducted on three different clay-based natural geological barrier materials: (i) Boom Clay, (ii) Callovo-Oxfordian claystone and (iii) Mercia Mudstone/microsparstone. Further details relating to these samples are given in the following sections, but a summary of their geotechnical properties is also given in Table 1. To minimise possible osmotic swelling of samples, a synthetic porewater solution was prepared for use as the backpressure fluid and as the permeant during all hydraulic testing. In the absence of pore-fluid composition data for the Mercia mudstone, a salt-saturated solution was made using crushed halite from close in the succession to the sampling location (Harrington et al., 2018). Each test consisted of a hydration phase, an initial hydraulic test and a consolidation phase.

Figure 1. A sample of Mercia Mudstone after preparation (left), arranged within the isotropic test assembly (centre) and as a 2D x-ray image (right).

Table 1. Geotechnical properties of test samples used to provide experimental data for model validation. In the absence of test data, values marked # are based on average values quoted by Harrington et al. (2017).

Sample	Length [mm]	Diameter [mm]	Bulk density [Mg.m^{-3}]	Dry density [Mg.m^{-3}]	Void ratio [-]
Boom Clay	42.67	49.92	2.05	1.68	0.60
Callovo-Oxfordian	48.38	50.18	2.45#	2.32#	0.17#
Mercia Mudstone	48.76	54.42	2.32	2.10	0.30

3. Numerical model: linear elastic skeletal deformation

3.1 Governing equations

The fluid flow through a compressible porous medium may be described by Biot's model, see Biot (1941). In this model, the governing equation for flow is obtained by combining Darcy's law with the mass conservation equation, thus leading to

$$\nabla \cdot \left(\frac{k}{\mu} \nabla p\right) = \phi\beta \frac{\partial p}{\partial t} + \frac{\partial}{\partial t}(\nabla \cdot \boldsymbol{u}) \tag{1}$$

where $\boldsymbol{u}$ is the solid displacement [m], p is the fluid pressure [Pa], k is the intrinsic permeability [m^2], μ is the dynamic viscosity of the fluid [Pa·s], ϕ is the porosity [-] and β is the compressibility of the fluid [Pa^{-1}]. Note that an isotropic permeability, represented by the scalar k, is here assumed.

The classical Biot's model assumes an elastic deformation of the matrix. Thus, Equation (1) is coupled to the mechanical equilibrium equation

$$\nabla \cdot \boldsymbol{\tau} + \boldsymbol{f} = \boldsymbol{0} \tag{2}$$

where $\boldsymbol{f}$ is the body force per unit volume of the medium [N/m^2] and $\boldsymbol{\tau}$ is the total stress on the medium [Pa], which can be expressed as

$$\boldsymbol{\tau} = \boldsymbol{\sigma} - \alpha p \mathbf{I} \tag{3}$$

where $\boldsymbol{\sigma}$ is the effective stress tensor [Pa], α is the Biot's coefficient [-] and $\mathbf{I}$ is the identity tensor. Under the assumption of small strains and assuming an isotropic linear elastic material, the effective stress tensor takes the form

$$\boldsymbol{\sigma} = \lambda tr(\boldsymbol{\varepsilon})\mathbf{I} + 2G\boldsymbol{\varepsilon} \tag{4}$$

where λ is the first Lamé's constant [Pa], G is the shear modulus [Pa] and tr stands for the trace operator. For the sake of simplicity, $\alpha = 1$ is here assumed. This is a reasonable assumption for a saturated porous medium and leads to the equation

$$\frac{E}{2(1+\nu)(1-2\nu)} \nabla(\nabla \cdot \boldsymbol{u}) + \frac{E}{2(1+\nu)} \nabla^2 \boldsymbol{u} - \nabla p = -\boldsymbol{f} \tag{5}$$

where E is the Young's modulus [Pa] and ν is the Poisson's coefficient [-]. Note that the relationships $\boldsymbol{\varepsilon} = \nabla^s \boldsymbol{u},\ \lambda = \frac{E\nu}{(1+\nu)(1-2\nu)}$ and $G = \frac{E}{2(1+\nu)}$ have here been used.

3.2 Finite element formulation

The numerical solution of Biot's model is usually approached using the Galerkin finite element method. Thus, Equations (1) and (5) are first cast in a weak form to be subsequently linearised. Following standard procedures, the solid displacements and the fluid pressure at time t can be expressed as

$$\boldsymbol{u}(\boldsymbol{x}) \cong \mathbf{u}^h(\boldsymbol{x}) = \mathbf{N}(\boldsymbol{x})\mathbf{u} \tag{6.1}$$

$$p(\boldsymbol{x}) \cong \mathbf{p}^h(\boldsymbol{x}) = \mathbf{N}(\boldsymbol{x})\mathbf{p} \tag{6.2}$$

where $\mathbf{N}$ is the matrix of standard finite element shape functions, $\mathbf{u}$ is the standard nodal displacement vector and $\mathbf{p}$ is the standard fluid pressure vector. These approximations lead to the coupled-system of discretized equations

$$\mathbf{L}^{\mathrm{T}} \frac{d\mathbf{u}}{dt} + \mathbf{H}\mathbf{p} + \mathbf{S}\frac{d\mathbf{p}}{dt} = -\mathbf{F}_{\mathbf{p}} \tag{7.1}$$

$$\mathbf{K}\mathbf{u}^{n+1} - \mathbf{L}\mathbf{p}^{n+1} = \mathbf{F}_{\mathbf{u}} \tag{7.2}$$

which upon application of the backward Euler finite difference time scheme becomes

$$\begin{bmatrix} \mathbf{K} & -\mathbf{L} \\ \mathbf{L}^{\mathrm{T}} & \Delta t\mathbf{H}+\mathbf{S} \end{bmatrix} \cdot \begin{bmatrix} \mathbf{u}^{n+1} \\ \mathbf{p}^{n+1} \end{bmatrix} = \begin{bmatrix} \mathbf{F}_{\mathbf{u}} \\ \mathbf{L}^{\mathrm{T}}\mathbf{u}^n + \mathbf{S}\mathbf{p}^n - \Delta t\mathbf{F}_{\mathbf{p}} \end{bmatrix} \tag{8}$$

In order to obtain a symmetric system, here the sign convention normally adopted for the variable $\mathbf{p}$ is reversed. Hence, for the coupled problem of flow through a deformable medium, $\mathbf{p}$ is negative for compressive pressure whereas it is positive for tensile pressure thus leading to the system

$$\begin{bmatrix} \mathbf{K} & \mathbf{L} \\ \mathbf{L}^{\mathrm{T}} & -\Delta t\mathbf{H}-\mathbf{S} \end{bmatrix} \cdot \begin{bmatrix} \mathbf{u}^{n+1} \\ \mathbf{p}^{n+1} \end{bmatrix} = \begin{bmatrix} \mathbf{F}_{\mathbf{u}} \\ \mathbf{L}^{\mathrm{T}}\mathbf{u}^n - \mathbf{S}\mathbf{p}^n + \Delta t\mathbf{F}_{\mathbf{p}} \end{bmatrix} \tag{9}$$

with the matrices defined in Table 2.

Table 2. Block matrices of the discretized Biot's system of equations.

Matrix	**Symbol**	**Expression**
Flux matrix	$\mathbf{F_p}$	$\mathbf{F_p} = \int_{\Gamma_\mathbf{p}} \mathbf{N}^\mathrm{T}\mathbf{q}\,\mathrm{d}\Omega$, where **q** is the flux vector prescribed on the boundary $\Gamma_\mathbf{p}$.
Load matrix	$\mathbf{F_u}$	$\mathbf{F_u} = \int_{\Gamma_\mathbf{u}} \mathbf{N}^\mathrm{T}\mathbf{t}\,\mathrm{d}\Omega$, where **t** is the traction vector prescribed on the boundary $\Gamma_\mathbf{u}$.
Permeability matrix	**H**	$\mathbf{H} = \int_\Omega (\nabla\mathbf{N})^\mathbf{T}\frac{k}{\mu}\nabla\mathbf{N}\,\mathrm{d}\Omega$
Soil stiffness matrix	**K**	$\mathbf{K} = \int_\Omega \mathbf{B}^\mathbf{T}\mathbf{CB}\,\mathrm{d}\Omega$, where **B** is the matrix of shape function derivatives and **C** is the elastic stiffness tensor.
Coupling matrix	**L**	$\mathbf{L} = \int_\Omega \mathbf{B}^\mathrm{T}\mathbf{mN}\,\mathrm{d}\Omega$, where $\mathbf{m} = [1,1,1,0,0,0]^\mathrm{T}$.
Compressibility matrix	**S**	$\mathbf{S} = \int_\Omega \mathbf{N}^\mathrm{T}\phi\beta\mathbf{N}\,\mathrm{d}\Omega$

3.3 Model parametrization: Young’s modulus and permeability estimation

The coupled system of equations (9) can be solved to estimate the rock properties (namely the hydraulic permeability and the Young’s modulus) of geological materials subjected to a consolidation test. As shown by Horseman et al. (2005), Biot’s model is unable to represent multiple testing stages from a single set of material values. Thus, for each material, each consolidation stage is treated here as a separate test and the fitting procedure of Table 3 is applied. Due to the nature of this problem, a two-dimensional axisymmetric finite element model is used here (Figure 2).

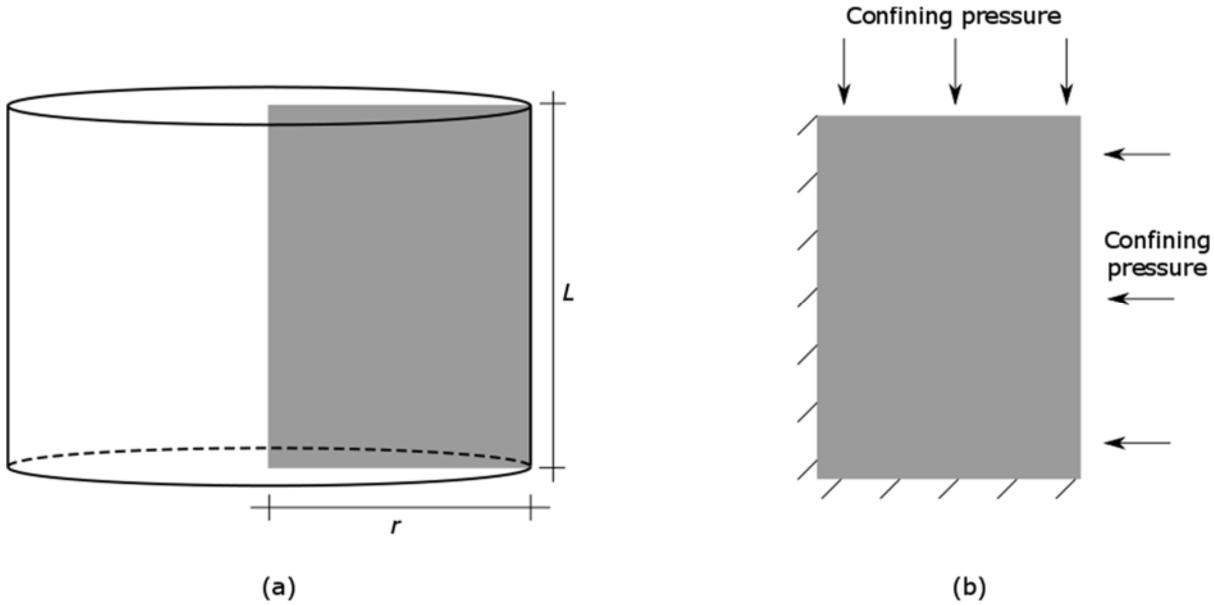

Figure 2. Schematic diagram of the main elements of (a) the axisymmetric plane for the numerical calculations and (b) the prescribed boundary conditions.

Table 3. Iterative algorithm to fit the Young's modulus and the permeability, given experimental outflow curves.

Algorithm 1: Fitting procedure to determine E and k, assuming a linear elastic skeleton deformation

---

Requires: experimental data (outflow f_{exp} versus time curve)

1: generate a two-dimensional finite element mesh (radius and length of the sample are required).

2: prescribe the *fixed* material parameters: that is, the Poisson's coefficient (ν), the dynamic viscosity (μ) and the specific storage (S_s).

3: define initial values E_0, k_0 for the two fitting parameters.

4: define a time discretization.

5: compute the constant block matrices of Table 2 (flux, load and coupling matrices).

6: compute the initial permeability matrix $\mathbf{H}_0 = \int_\Omega (\nabla\mathbf{N})^{\mathbf{T}} \frac{k_0}{\mu} \nabla\mathbf{N}\, \mathrm{d}\Omega$.

7: compute the initial stiffness matrix $\mathbf{K}_0 = \int_\Omega \mathbf{B}^{\mathbf{T}}\mathbf{C}_0\mathbf{B}\, \mathrm{d}\Omega$, with $\mathbf{C}_0 = \mathbf{C}(E_0, \nu)$.

8: compute the initial compressibility matrix $\mathbf{S}_0 = \int_\Omega \mathbf{N}^{\mathrm{T}}(\phi\beta)_0\mathbf{N}\, \mathrm{d}\Omega$, with

$$(\phi\beta)_0 = \frac{S_s}{\rho_w g} - \alpha_0$$

where ρ_w is the pore-water density [kg/m^3], g is the gravitational acceleration (=9.81 m/s^2) and $\alpha_0 = 3\frac{1-2\nu}{E_0}$ is the initial solid-phase compressibility [Pa^{-1}].

9: solve coupled system of equations (9).

10: compute the numerical outflow f_{num}^0.

11: iteratively update E in such a way as to minimise the difference between the numerical and the experimental outflows at time $t = t_{\text{end}}$.

12: iteratively update k in such a way as to minimise the difference between the numerical and the experimental transient phases of the outflow versus time curves.

Note that in Algorithm 1 the facts that (a) the Young's modulus mainly determines the total volume of fluid expelled (line 11) and (b) the permeability mainly determines the rate at which fluid is expelled (line 12) have been used, (Figure 3).

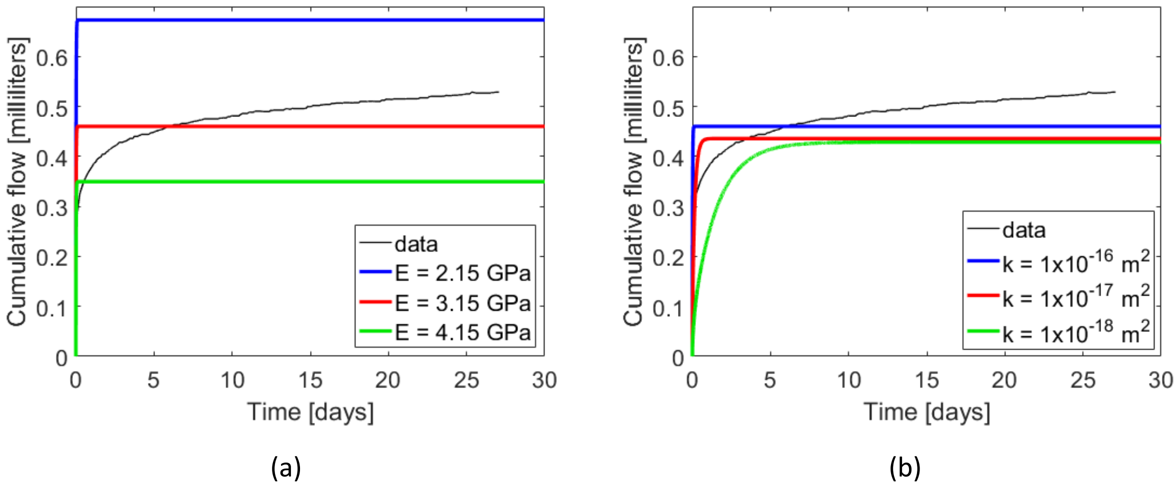

Figure 3. Synthetic example: numerical outflow versus time curves obtained with (a) three different Young's modulus and the rest of parameters kept constant and (b) three different permeability values and the rest of parameters kept constant. In black, experimental data from Harrington et al. (2018) measured for the Mercia Mudstone Group sample is shown.

This fitting algorithm provided reasonable theoretical flow-time curves for three Mercia Mudstone Group samples, see Harrington et al. (2018). However, as highlighted there and as seen in the synthetic example of Figure 3, Biot's model is unable to reproduce the time-dependent behaviour of the flow versus time curve. Thus, a more complex deformation model, allowing for this creep effect needs to be considered.

4. Numerical model: time-dependent skeletal deformation

In each consolidation stage, the stress is raised abruptly and then kept constant. The initial instantaneous increase in the confining stress (from $\boldsymbol{\sigma}_0$ to $\boldsymbol{\sigma}_f$) leads to an immediate increase of the strain (from $\boldsymbol{\varepsilon}_0$ to $\boldsymbol{\varepsilon}_f$) causing an instantaneous flow expulsion. This initial behaviour is observed in the experimental flow versus time curves (Figure 3) and can be successfully described with a linear elastic behaviour. However, a further flow ejection period also occurs once the confining stress is kept constant. This results from strain increasing further with time, despite the constant stress. This time-dependent behaviour is shown by viscoelastic materials and can be modelled by assuming a time-dependent Young's modulus at constant stress. Particularly, in a one-dimensional setting,

$$E(t) = \frac{\sigma}{\varepsilon(t)} \tag{10}$$

where the deformation (and thus $E(t)$) approaches a constant value when the loading time becomes large, see Figure 4.

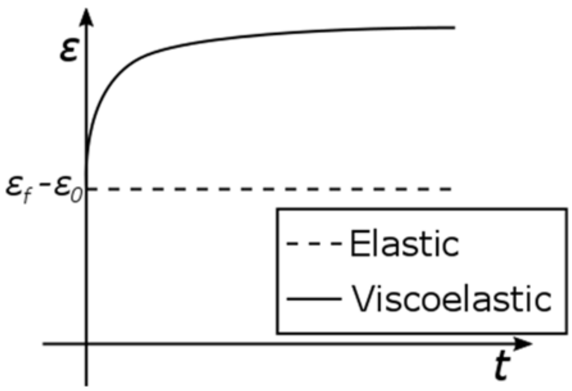

Figure 4. Strain versus time curve at constant stress for an elastic and a viscoelastic material.

4.1. Creep modulus: standard solid element

Different mathematical expressions for the time-dependent Young's modulus $E(t)$ may be employed. However, classical linear viscoelastic models assume that materials behave as one-dimensional spring-dashpot systems (Figure 5). For the sake of simplicity, two-element models are preferred here. Nevertheless, the Maxwell model does not describe an anelastic recovery (Figure 5a), whereas the Kelvin-Voigt model (Figure 5b), does not predict an instantaneous strain. Thus, the standard solid model (Figure 5c) is adopted here, which leads to a creep compliance

$$J(t) = \frac{1}{E_\infty} + \frac{1}{E_1}\left(1 - e^{-\frac{\eta_1}{E_1}t}\right) \tag{11}$$

and to a time-dependent elastic modulus

$$E(t) = \frac{1}{\frac{1}{E_\infty}+\frac{1}{E_1}\left(1-e^{-\frac{\eta_1}{E_1}t}\right)} \tag{12}$$

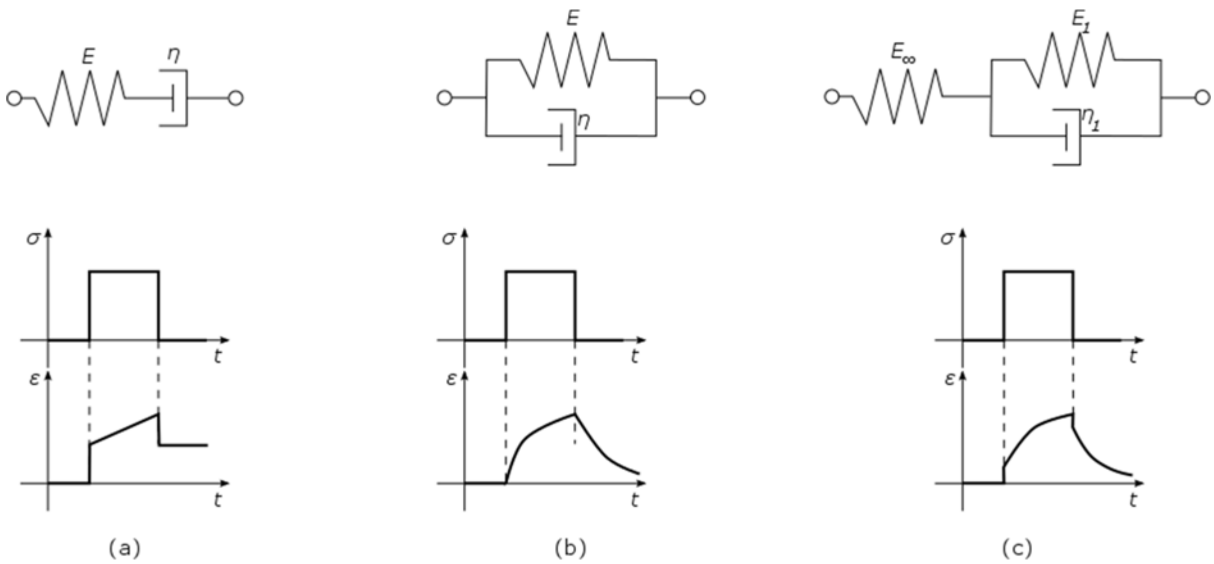

Figure 5. Time response of the strain in a creep experiment for a (a) Maxwell model, (b) Kelvin-Voigt model and (c) standard solid.

Note that by means of this viscoelastic model, the fitting complexity increases: in the elastic model, one mechanical parameter (E) is required while in the linear viscoelastic model, three new mechanical values (E_∞, E_1 and η_1) need to be estimated. In order to reduce this complexity,

$$E \coloneqq E_\infty = E_1 \tag{13}$$

is here prescribed. Hence, the time-dependent Young's modulus (12) may be expressed as

$$E(t) = \frac{E}{2-e^{-at}} \tag{14}$$

where $a \coloneqq \eta_1/E$ [s^{-1}] is here used.

This enhancement in the mechanical properties of the material leads to a time-dependent elastic stiffness tensor and to a time-dependent fluid storage coefficient. Thus, the coupled system (9) is now

$$\begin{bmatrix} \mathbf{K}^{n+1} & \mathbf{L} \\ \mathbf{L}^{\mathrm{T}} & -\Delta t\mathbf{H}\text{-}\mathbf{S}^{n+1} \end{bmatrix} \cdot \begin{bmatrix} \mathbf{u}^{n+1} \\ \mathbf{p}^{n+1} \end{bmatrix} = \begin{bmatrix} \mathbf{F_u} \\ \mathbf{L}^{\mathrm{T}}\mathbf{u}^{n} - \mathbf{S}^{n+1}\mathbf{p}^{n} + \Delta t\mathbf{F_p} \end{bmatrix} \tag{15}$$

with

$$\mathbf{K}^i = \int_\Omega \mathbf{B}^{\mathbf{T}}\mathbf{C}^i\mathbf{B}\,\mathrm{d}\Omega \tag{16a}$$

$$\mathbf{S}^i = \int_\Omega \mathbf{N}^{\mathrm{T}}(\phi\beta)^i\mathbf{N}\,\mathrm{d}\Omega \tag{16b}$$

where $\mathbf{C}^i = \mathbf{C}(\mathrm{E}(t^i), \nu)$ and $(\phi\beta)^i = \frac{S_s}{\rho_w g} - 3\frac{1-2\nu}{E(t^i)}$ stand for the elastic stiffness and the fluid storage coefficient at time step i respectively.

4.2. Model parametrization: spring stiffness, dashpot viscosity and permeability

The coupled system of equations (15) can be solved to estimate the new rock properties. If the viscoelastic model with the time-dependent Young's modulus (14) is assumed, three parameters are needed: E, a and k. Here, the fitting procedure of Table 4 is proposed. Again, as done in Section 3.3 for the elastic material, each consolidation stage is treated as a separate test.

Table 4. Iterative algorithm to fit the time-dependent Young's modulus and the permeability, given experimental outflow curves.

Algorithm 2: Fitting procedure to determine E, a, k assuming a viscoelastic skeleton deformation
Requires: experimental data (outflow f_{exp} versus time curve)
generate a two-dimensional finite element mesh (radius and length of the sample are required).

2: prescribe the *fixed* material parameters: that is, the Poisson's coefficient (ν), the dynamic viscosity (μ) and the specific storage (S_s).
3: define initial values E_0, a_0, k_0 for the three fitting parameters.
4: define a time discretization.
5: compute the constant block matrices of Table 2 (flux, load and coupling matrices).
6: compute the initial permeability matrix $\mathbf{H}_0 = \int_\Omega (\nabla \mathbf{N})^{\mathbf{T}} \frac{k_0}{\mu} \nabla \mathbf{N}\, d\Omega$.
7: compute the initial stiffness matrix $\mathbf{K}_0^0 = \int_\Omega \mathbf{B}^{\mathbf{T}} \mathbf{C}_0^0 \mathbf{B}\, \mathrm{d}\Omega$, with $\mathbf{C}_0^0 = \mathbf{C}^0(E(E_0, a_0, t^0), \nu)$.
8: compute the initial compressibility matrix $\mathbf{S}_0^0 = \int_\Omega \mathbf{N}^{\mathrm{T}} (\phi\beta)_0^0 \mathbf{N}\, d\Omega$, with

$$(\phi\beta)_0^0 = \frac{S_s}{\rho_w g} - 3\frac{1-2\nu}{E(E_0, a_0, t^0)}$$

9: solve coupled system of equations (15). Thus, at each time step, the stiffness and compressibility matrices are updated.
10: compute the numerical outflow f_{num}^0.
11: iteratively update E in such a way as to minimise the difference between the numerical and the experimental outflows at time $t = t_{\mathrm{end}}$.
12: iteratively update a in such a way as to minimise the difference between the numerical and the experimental outflow slopes (after the initial instantaneous flow expulsion).
13: iteratively update k in such a way as to minimise the difference between the numerical and the experimental transient phases of the outflow versus time curves.

Note that now, the total volume of fluid expelled is controlled by both the spring stiffness E and the numerical parameter a. However, as seen in Figure 6, each of these two parameters has a different physical value. Indeed, E mainly determines the total volume of fluid expelled after the instantaneous flow expulsion whereas a controls the slope of the time-dependent branch. This has been taken into account in Algorithm 2 (see lines 11 and 12, respectively).

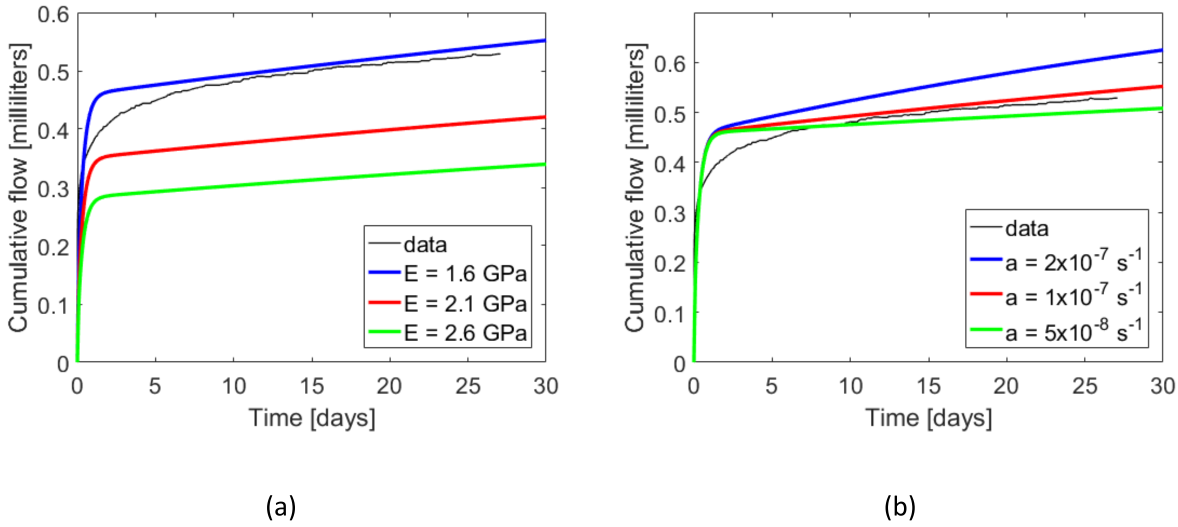

Figure 6. Synthetic example: numerical outflow versus time curves obtained with (a) three different values for the spring stiffness and the rest of parameters kept constant and (b) three different values of a and the rest of parameters kept constant. In black, experimental data from Harrington et al. (2018) measured for the Mercia Mudstone Group sample is shown.

5. Results: validation of the numerical model

The new numerical model is validated against different experimental results conducted at the British Geological Survey (BGS). To illustrate the generality of the strategy, three different materials are here analysed: (a) a Boom Clay sample extracted from the High Activity Experimental Site (HADES) Underground Research Laboratory (URL) at Mol in Belgium, (b) a Callovo-Oxfordian claystone (COx) specimen taken from the Meuse/Haute Marne URL in France and (c) a mudstone sample of the Mercia Mudstone Group collected from a halite mine in Northern Ireland. These materials differ in their clay content and thus, their physical properties such as rock porosity and permeability are significantly different: clay-rich samples are characterised by smaller pore-throats and thus by lower permeability values.

5.1 Boom Clay specimen

The first test relates to a Boom Clay sample extracted from the HADES Underground Research Laboratory (URL) at Mol in Belgium (Figure 7). This specimen was taken from a location 223 m below surface within the research facility. At depth this material can be described as a hard, high plasticity clay, see Horseman et al. (1987). It is of interest in Belgium and the Netherlands as potential host formation for a radioactive waste disposal facility.

Figure 7. Isotropic test assembly containing the Boom Clay sample.

Following assembly of the apparatus, an initial equilibration period of 8 days was applied to the cylindrical sample, with confining pressure held constant at 4.4 MPa. The pore pressure within the sample was then allowed to equilibrate, with both the injection and backpressure ends being held at a constant condition of 2.2 MPa. These conditions were selected to return the clay to those experienced *in situ* prior to exhumation. Once the equilibration stage (stage [0]) was complete, a ten-step consolidation test was performed, see Table 5 and Figure 8. As seen, the injection and backpressure were held constant at 2.7 MPa and 2.2 MPa respectively during the entire consolidation period, ensuring a constant flow of water across the sample. Instantaneous flow rate and net cumulative flow volume data were collected, with the latter equating to volumetric strain. Estimated specific storage values, see Table 5, are here used to validate the proposed strategy.

Table 5. Summary of experimental histories for the Boom Clay sample.

BOOM CLAY SAMPLE				
Stage number	**Confining pressure [MPa]**	**Injection pressure [MPa]**	**Backpressure [MPa]**	**Specific storage [m^{-1}]**
1	6.4	2.7	2.2	5.1×10^{-5}
2	8.4	2.7	2.2	13.7×10^{-5}
3	10.4	2.7	2.2	27.0×10^{-5}
4	8.4	2.7	2.2	3.5×10^{-5}
5	6.4	2.7	2.2	6.0×10^{-5}
6	4.4	2.7	2.2	10.9×10^{-5}
7	6.4	2.7	2.2	7.8×10^{-5}
8	8.4	2.7	2.2	7.2×10^{-5}
9	10.4	2.7	2.2	7.6×10^{-5}
10	12.4	2.7	2.2	12.7×10^{-5}

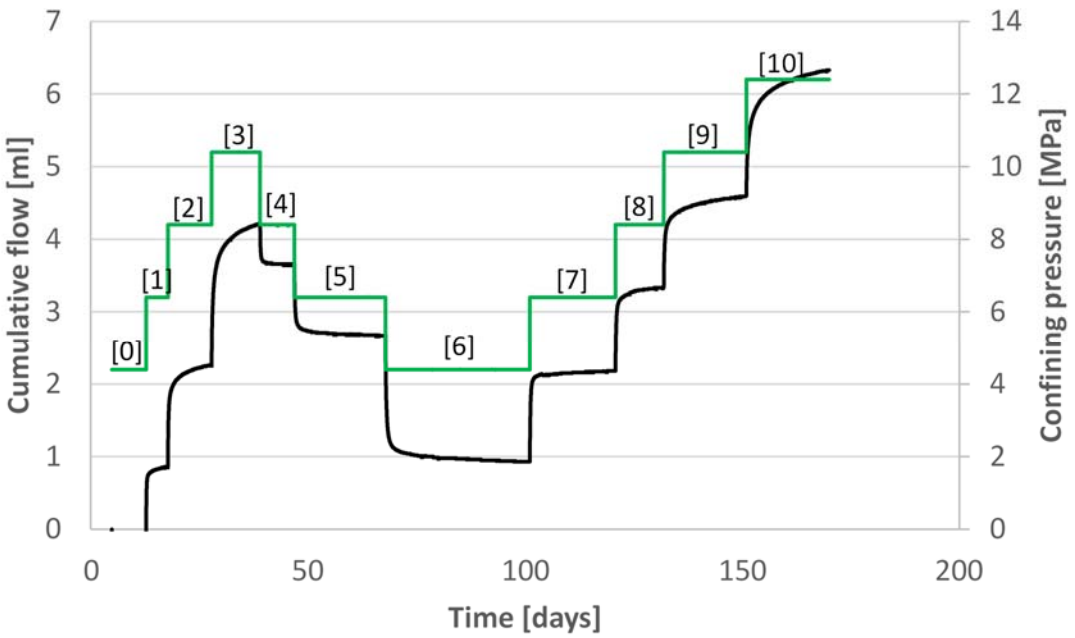

Figure 8. Boom Clay sample: cumulative flow (in black) and confining systems (in green) from test stages [1]-[10].

Analysis of the consolidation data is here performed by assuming both an elastic and a viscoelastic skeletal deformation. Here, the geometrical and material parameters of Table 6 are used. As seen, the Poisson's coefficient reported by Barnichon and Volckaert (2003) and Bésuelle et al. (2013) is used here.

Table 6. Geometrical and material parameters used in the numerical fittings for the Boom Clay specimen.

BOOM CLAY SAMPLE		
Meaning	**Symbol [units]**	**Value**
Radius of the sample	r [mm]	24.96
Length of the sample	L [mm]	42.67
Poisson's coefficient	ν [-]	0.125
Dynamic viscosity	μ [Pa · s]	2.32×10^{-3}

As done in Horseman et al. (2005), each consolidation stage is treated here as a separate test. The fitting results are shown in Figure 9. As seen, the elastic model (blue-dotted curve) is not able to represent the time-dependent behaviour observed experimentally in some consolidation stages, whereas laboratory data fit better with the proposed viscoelastic model (red-dashed curve). The fitted parameters obtained with both models are listed in Table 7 and Figure 10. As seen, the two models lead to a similar Young's modulus. This is in agreement with the suggested definition of the time-dependent Young's modulus, see Equation 14, since the evolving Young's modulus tends to the elastic one when the loading time becomes large enough. However, the new model does lead to significantly improved permeability value predictions, especially for those stages where the confining pressure decreased.

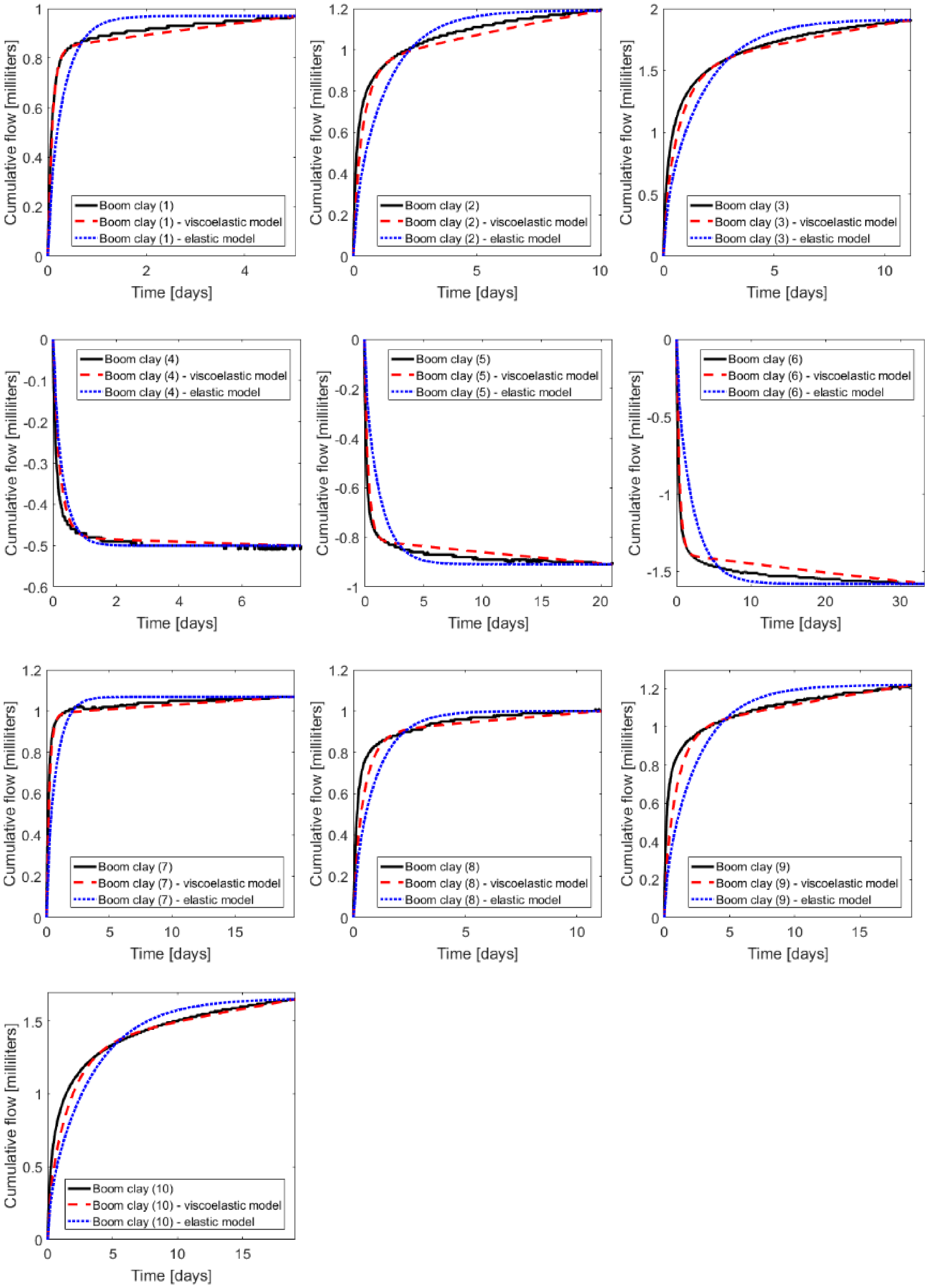

Figure 9. Boom Clay specimen: comparison of model to flow data.

Table 7. Boom Clay specimen: parameter values determined for each stage.

BOOM CLAY SAMPLE						
	EXPERIMENTAL		FITTED			
			ELASTIC SKELETAL DEFORMATION		VISCOELASTIC SKELETAL DEFORMATION	
Stage number	Permeability [m^2]	Young's Modulus [MPa]	Permeability [m^2]	Young's Modulus [MPa]	Permeability [m^2]	(Averaged) Young's Modulus [MPa]
1	1.44×10^{-19}	581.82	7.73×10^{-20}	351.10	3.44×10^{-19}	413.29
2	1.17×10^{-19}	221.01	4.92×10^{-20}	276.83	1.71×10^{-19}	321.85
3	8.33×10^{-19}	114.84	7.34×10^{-20}	171.15	1.77×10^{-19}	192.93
4	9.04×10^{-20}	846.02	5.77×10^{-20}	908.58	8.65×10^{-20}	950.87
5	1.03×10^{-19}	486.29	2.31×10^{-20}	467.43	1.00×10^{-19}	533.69
6	1.25×10^{-19}	263.08	2.43×10^{-20}	268.06	1.60×10^{-19}	316.09
7	1.11×10^{-19}	385.61	4.91×10^{-20}	315.51	1.94×10^{-19}	357.87
8	9.59×10^{-20}	413.78	3.37×10^{-20}	334.20	7.43×10^{-20}	363.93
9	8.09×10^{-20}	393.46	1.37×10^{-20}	262.60	3.73×10^{-20}	292.92
10	5.70×10^{-20}	236.86	1.76×10^{-20}	192.40	3.62×10^{-20}	211.45

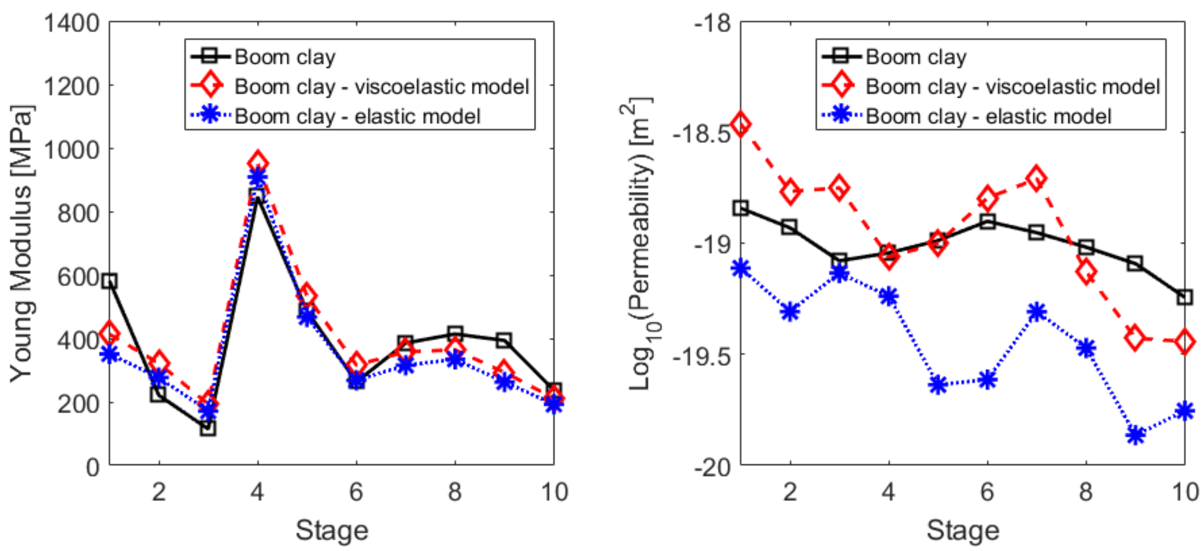

Figure 10. Boom Clay specimen: parameter values determined for each stage.

5.2 Callovo-Oxfordian claystone

The second test was conducted on a sample of the Callovo-Oxfordian claystone (COx) collected from a location 450 m below surface at the Meuse/Haute Marne URL (France), see Figure 11. The COx is of interest in France as a candidate host formation for a radioactive waste disposal facility. A six-step consolidation test was carried out after an initial equilibration period of 62 days, with the confining pressure held at 9 MPa, see Figure 12, and the pore pressure at 1.0 MPa. As seen in Table 8, the injection and backpressure during the entire consolidation period were held constant at 4.0 MPa and 1.0 MPa respectively, leading to a pore pressure gradient and continuous flow of water across the sample. Estimated specific storage values are here prescribed. For a detailed description of the test, see the report by Harrington and Tamayo-Mas (2016).

Figure 11. Sample of the Callovo-Oxfordian claystone.

Table 8. Summary of experimental histories for the COx sample.

CALLOVO-OXFORDIAN CLAYSTONE				
Stage number	**Confining pressure [MPa]**	**Injection pressure [MPa]**	**Backpressure [MPa]**	**Specific storage [m^{-1}]**
1	18.5	4.0	1.0	4.6×10^{-6}

2	28	4.0	1.0	3.8 x 10^{-6}
3	37.5	4.0	1.0	5.0 x 10^{-6}
4	47	4.0	1.0	4.7 x 10^{-6}
5	56.5	4.0	1.0	6.4 x 10^{-6}
6	66	4.0	1.0	6.5 x 10^{-6}

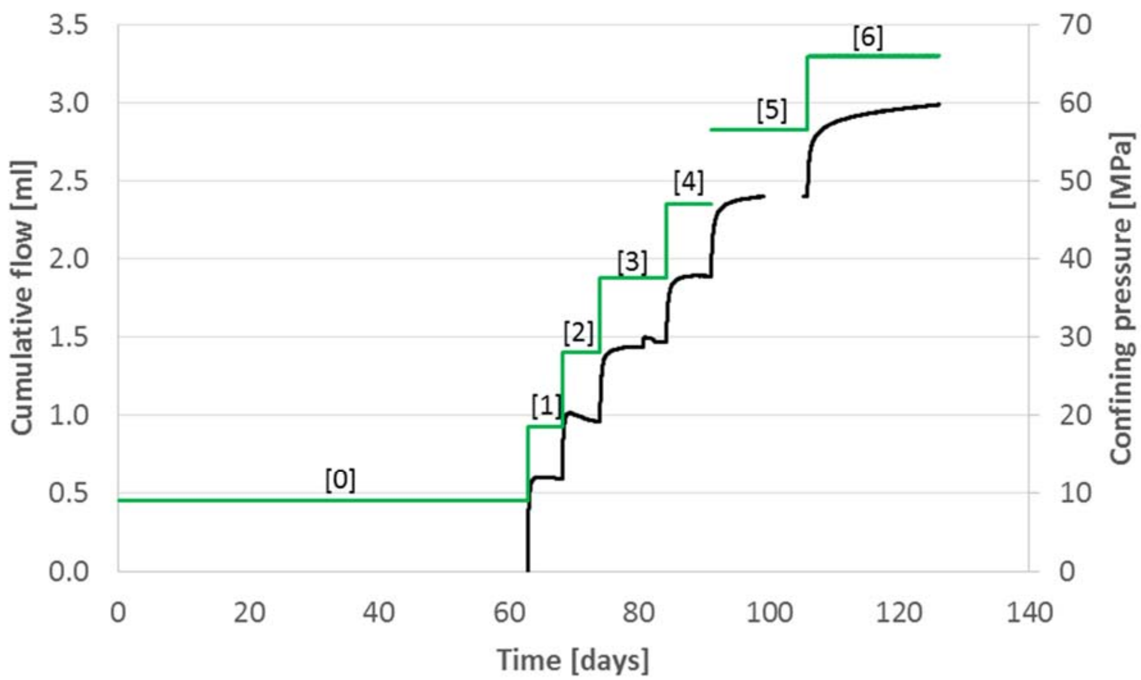

Figure 12. COx: cumulative flow (in black) and confining systems (in green) from test stages [1]-[6].

As for the Boom Clay sample, the consolidation data is analysed here by means of the elastic and viscoelastic models. The geometrical and material parameters used in the numerical simulations are shown in Table 9. Here, as with Harrington et al. (2018), the Poisson's ratio value reported by Wileveau and Bernier (2008) is used. The fitting results obtained with both models are shown in Figure 13. As seen, enhancing the elastic bulk with a dashpot viscosity leads to better fitting in those cases where the elastic model is not appropriate (see consolidation stages 3 and 6) and provides a very similar solution when yield has been reached and thus, the traditional model is acceptable (see consolidation stages 1, 4 and 5). As observed for the Boom

Clay sample, this improvement is especially significant for the permeability parameter, see Table 10 and Figure 14. The unusual form of the experimental data obtained for stage 2 (Figure 13), is due to a mismatch between in- and outflow values and hence, the fitting is done at the end of this test stage.

Table 9. Geometrical and material parameters used in the numerical fittings for the COx specimen.

CALLOVO-OXFORDIAN CLAYSTONE		
Meaning	**Symbol [units]**	**Value**
Radius of the sample	r [mm]	25.09
Length of the sample	L [mm]	48.38
Poisson's coefficient	ν [-]	0.3
Dynamic viscosity	μ [Pa · s]	1.00 x 10^{-3}

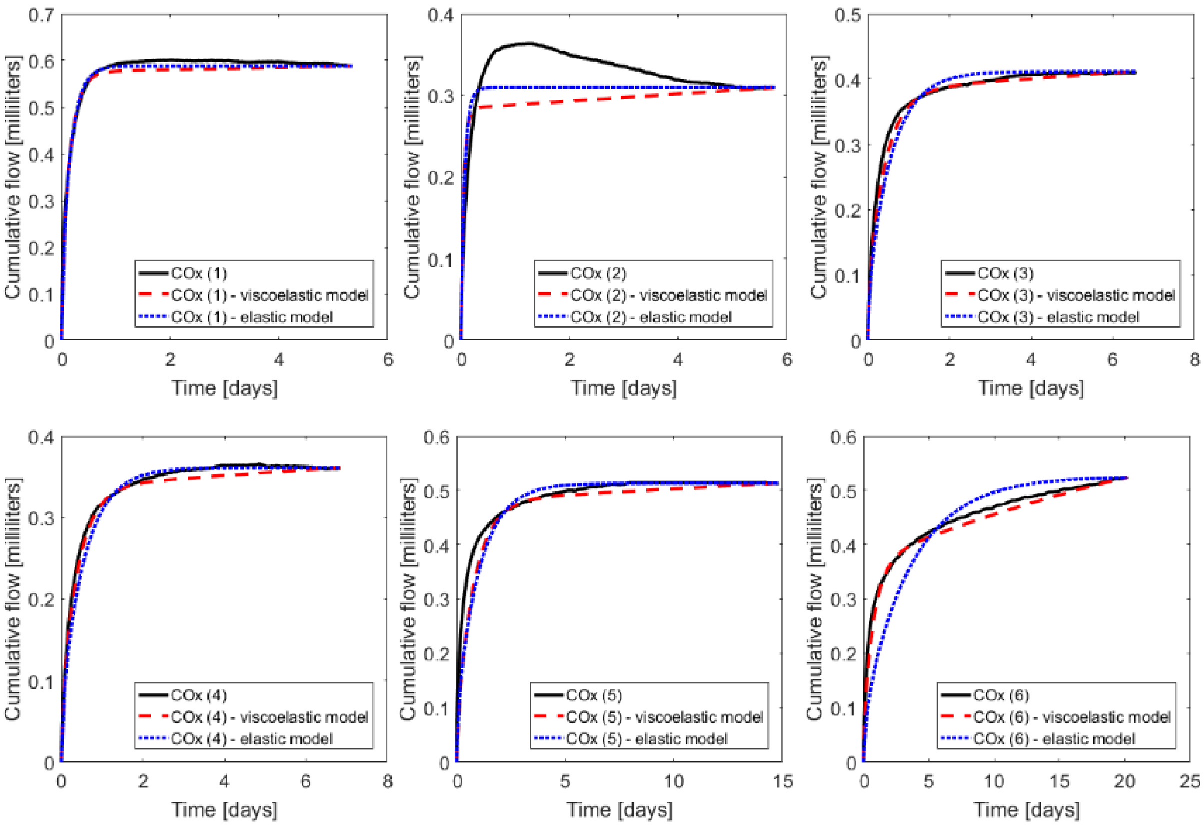

Figure 13. COx specimen: comparison of model to flow data.

Table 10. COx specimen: parameter values determined for each stage.

CALLOVO-OXFORDIAN CLAYSTONE						
Stage number	EXPERIMENTAL		FITTED			
			ELASTIC SKELETAL DEFORMATION		VISCOELASTIC SKELETAL DEFORMATION	
	Permeability [m^2]	Young's Modulus [GPa]	Permeability [m^2]	Young's Modulus [GPa]	Permeability [m^2]	(Averaged) Young's Modulus [GPa]
1	5.46 x 10^{-21}	3.60	8.30 x 10^{-21}	2.24	9.02 x 10^{-21}	2.27
2	4.91 x 10^{-21}	4.70	1.75 x 10^{-20}	4.61	2.63 x 10^{-20}	4.92
3	4.93 x 10^{-21}	3.53	2.33 x 10^{-21}	2.98	3.29 x 10^{-21}	3.10
4	4.03 x 10^{-21}	3.77	2.27 x 10^{-21}	3.48	3.27 x 10^{-21}	3.62
5	3.85 x 10^{-21}	2.77	1.66 x 10^{-21}	2.38	2.22 x 10^{-21}	2.49
6	3.88 x 10^{-21}	2.73	4.80 x 10^{-22}	2.29	2.25 x 10^{-21}	2.69

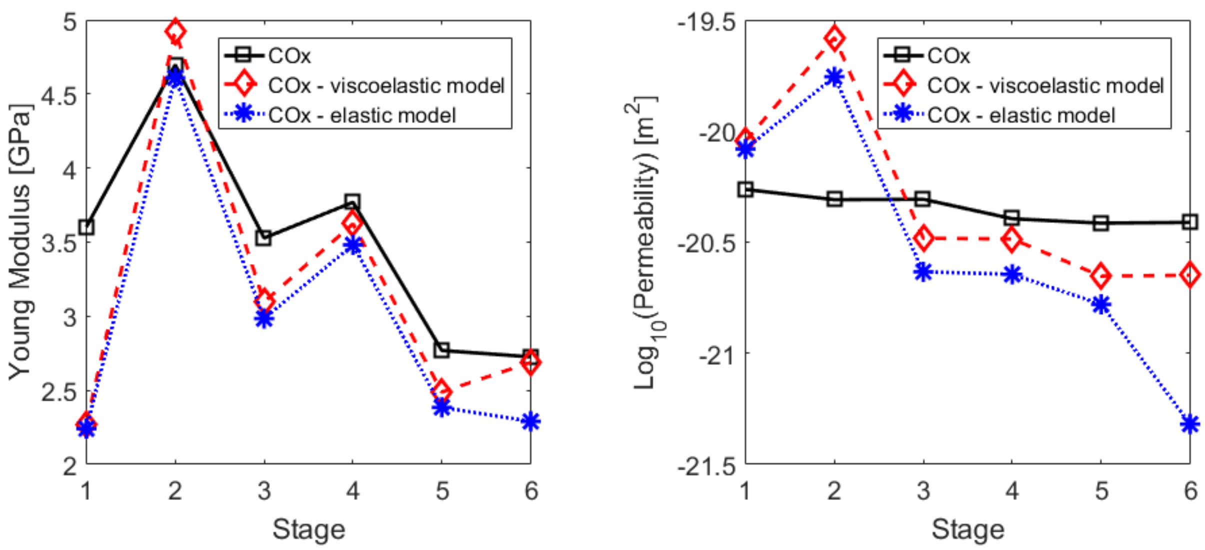

Figure 14. COx specimen: parameter values determined for each stage.

5.3 Mercia Mudstone formation sample

Thirdly, the approach is validated against a consolidation experiment conducted on a well-preserved sample recovered from the Knocksoghey Formation in the Larne Basin (Figure 15).

This sample was collected during excavation of a new mine drift in Northern Ireland within the Mercia Mudstone Group (MMG), which is of interest as a caprock for potential CO_2 storage sites in the North and Irish Seas, Armitage et al. (2013). This material can be described as a fine-grained mudstone to microsparstone, but it should be noted that at the microscopic scale it is highly heterogeneous. For a detailed description of the material, we refer to Harrington et al. (2018).

Figure 15. Sample from the Mercia Mudstone Group (left) and arranged with the isotropic test assembly (right).

After the initial equilibration period (confining stress and pore pressure were 14.0 MPa and 1.0 MPa respectively), the cylindrical specimen was subjected to a five-step consolidation test, see Figure 16 and Table 11. Here, no pore pressure difference across the sample was prescribed during consolidation.

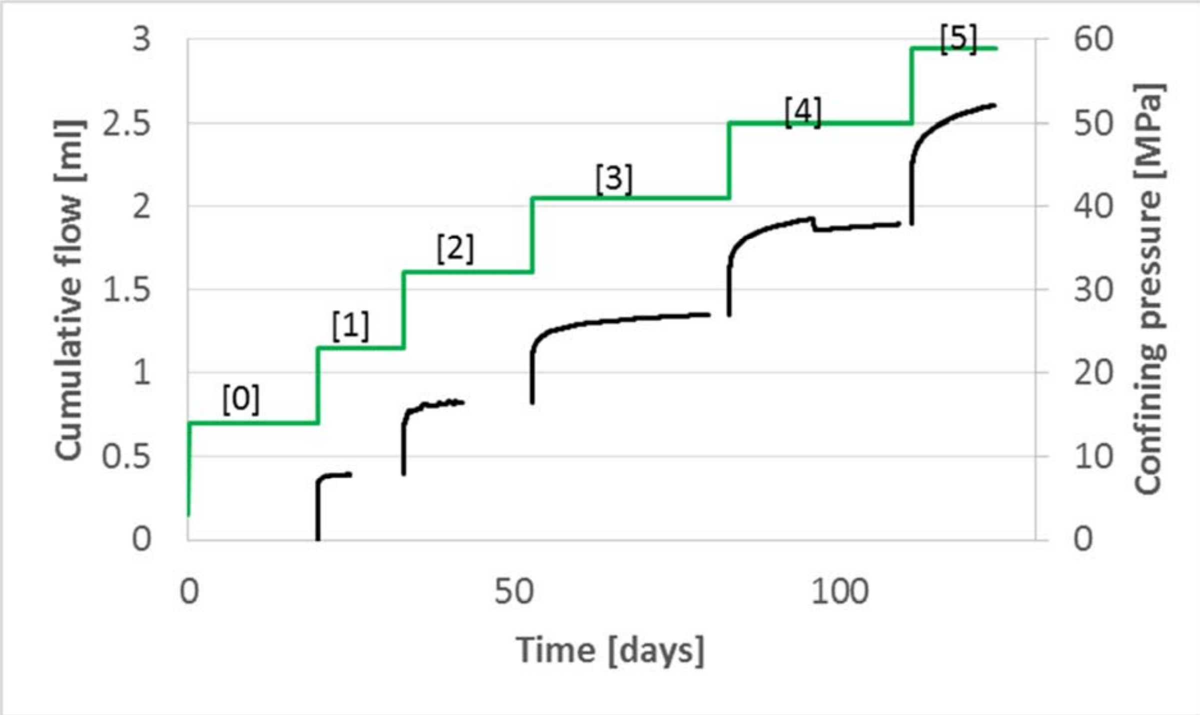

Figure 16. Mercia: cumulative flow (in black) and confining systems (in green) from test stages [1]-[5].

Table 11. Summary of experimental histories for the Mercia sample.

MERCIA MUDSTONE FORMATION SAMPLE			
Stage number	**Confining pressure [MPa]**	**Injection pressure [MPa]**	**Backpressure [MPa]**
1	23.0	1.0	1.0
2	32.0	1.0	1.0
3	41.0	1.0	1.0
4	50.0	1.0	1.0
5	59.0	1.0	1.0

As with the previous samples, the two suggested algorithms are here employed to derive the hydraulic and mechanical parameters. Here, the geometrical and material parameters of Table 12 have been used. As reported by Hobbs et al. (2002), Poisson's ratios for the MMG were found to vary from 0.2 and 0.4. Hence, an intermediate value $\nu = 0.25$ is considered here for all the numerical simulations. As seen, in this example, the specific storage has been considered constant during the entire consolidation process.

Table 12. Geometrical and material parameters used in the numerical fittings for the Mercia specimen.

MERCIA MUDSTONE FORMATION SAMPLE		
Meaning	**Symbol [units]**	**Value**
Radius of the sample	r [mm]	27.21
Length of the sample	L [mm]	48.76
Poisson's coefficient	ν [-]	0.25
Dynamic viscosity	μ [Pa · s]	2.32 x 10^{-3}
Specific storage	S_s [m^{-1}]	4.5 x 10^{-6}

The fittings are shown in Figure 17 and listed in Table 13. As seen, the new method is able to describe the experimental time-dependent behaviour also with this new material. Here, due to the high heterogeneity of the material, direct measurements of the permeability should be considered as indicative only. Thus, as with Harrington et al. (2018), numerical permeability values are compared here with the derived values

$$k = K \frac{\mu}{\rho_w \, g} \tag{17}$$

where μ is the dynamic viscosity of the fluid [Pa·s], ρ_w is the pore-water density [kg/m^3], g is the gravitational acceleration (=9.81 m/s^2) and K is the hydraulic conductivity [m/s]. Here, this value is estimated using the simple relationship

$$K = m_v c_v \gamma_v \tag{18}$$

where γ_v is the unit weight of water (=9.81 N/m^3), m_v is the coefficient of volume compressibility [Pa^{-1}] and c_v is the coefficient of consolidation [m^2/year], computed here by means of the Taylor's square root of time method, as described by Scott (1980). As seen in Figure 18, the proposed viscoelastic model leads to more accurate rock properties. However, as highlighted in Harrington et al. (2018) the experimental permeability values obtained for some stages (3,4,5) should be treated as indicative only as outflow had not fully asymptoted by the end of the stage.

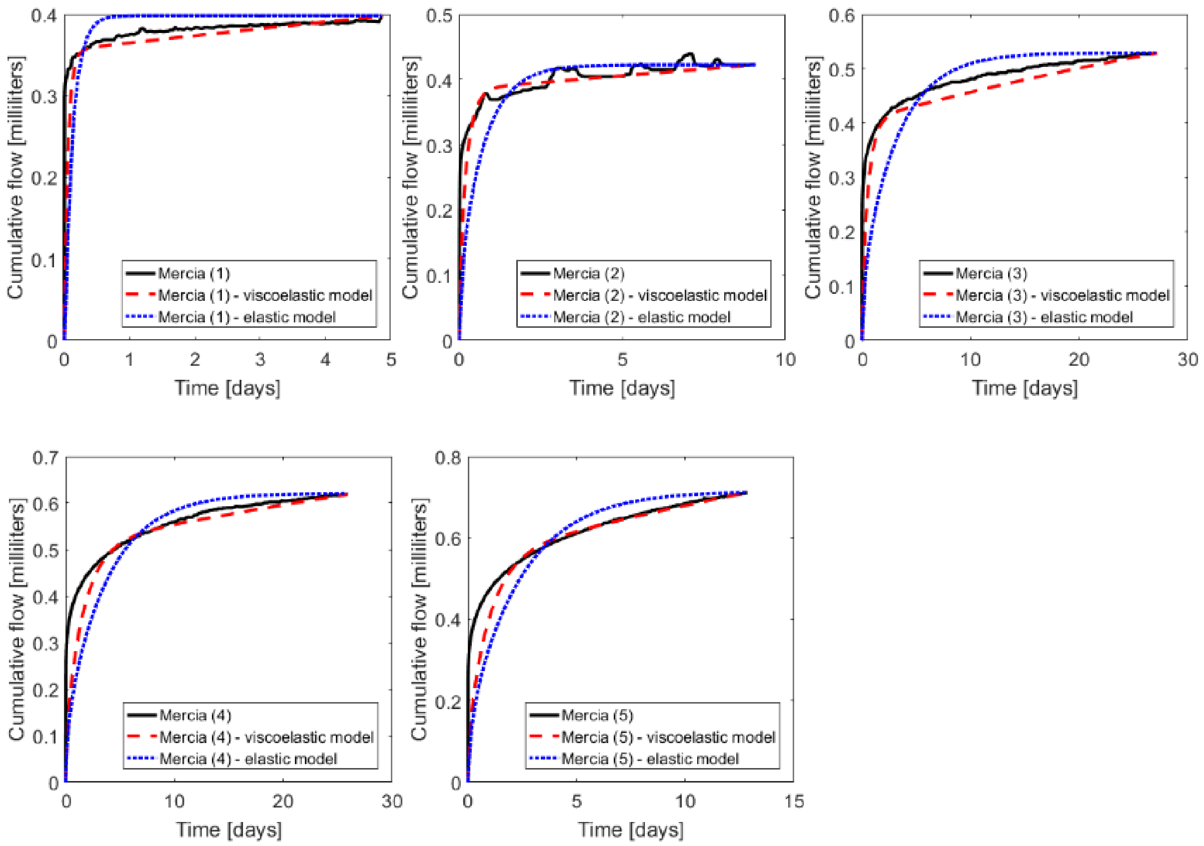

Figure 17. Mercia specimen: comparison of model to flow data.

Table 13. Mercia specimen: parameter values determined for each stage.

MERCIA MUDSTONE GROUP SAMPLE						
Stage number	**EXPERIMENTAL**		**FITTED**			
			ELASTIC SKELETAL DEFORMATION		**VISCOELASTIC SKELETAL DEFORMATION**	
	Permeability [m²]	**Young's Modulus [GPa]**	**Permeability [m²]**	**Young's Modulus [GPa]**	**Permeability [m²]**	**(Averaged) Young's Modulus [GPa]**
1	7.85×10^{-19}	3.937	7.06×10^{-20}	3.698	1.48×10^{-19}	3.731

2	1.33×10^{-19}	3.472	1.21×10^{-20}	3.058	3.56×10^{-20}	3.276
3	3.53×10^{-19}	2.758	3.44×10^{-21}	2.355	1.36×10^{-20}	2.813
4	4.25×10^{-20}	2.326	3.41×10^{-21}	1.972	4.49×10^{-21}	2.156
5	5.00×10^{-19}	2.007	6.10×10^{-21}	1.732	7.39×10^{-21}	1.881

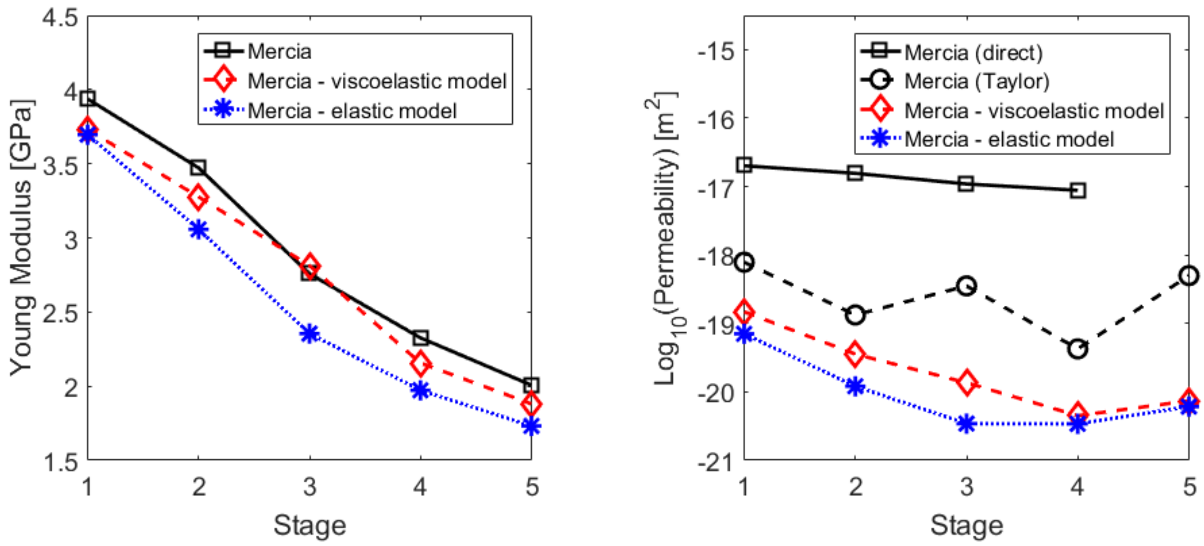

Figure 18. Mercia specimen: parameter values determined for each stage.

6 Conclusions

Biot's general consolidation theory is here enhanced to include the creep effect observed in experimental tests. The presented model assumes that the fluid flows through a viscoelastic medium, which has been modelled as a purely elastic spring connected in series with a Kelvin-Voigt model (another elastic spring connected in parallel with a dashpot). This is one of the simplest models that predicts an anelastic recovery together with an instantaneous strain. For the sake of simplicity, the elastic moduli of the two springs are here assumed to be equal thus leading to a minimal parametric uncertainty. Indeed, compared to the standard Biot's consolidation model, where two parameters need to be fitted from experimental observations, here three parameters are needed to describe the hydro-mechanical model:

- Two different parameters control the mechanical response of the material:

- The elastic modulus of the two springs, E, which mainly determines the total volume of fluid expelled after the instantaneous flow expulsion.
- The dashpot viscosity coefficient, η. The ratio η/E mainly controls the slope of the time-dependent branch.

- One parameter (the hydraulic permeability, k) controls the transient phase of the outflow versus time curve. This parameter has the same physical meaning as in the standard Biot's consolidation model.

The clear physical meaning of these parameters has been used here to derive two fitting algorithms: the former assumes the standard Biot's consolidation model whereas the latter, with only one extra line of pseudocode, is used for the viscoelastically-enhanced model.

The equations for this new model have been presented and implemented here within a finite element framework. As detailed, the proposed enhancement in the mechanical properties of the material leads to a time-dependent elastic stiffness tensor and to a time-dependent fluid storage coefficient. This procedure is thus computationally more demanding, but results in a more accurate hydro-mechanical model according to the experimental observations from different consolidation tests performed at the British Geological Survey:

- The enhanced model is able to better represent the consolidation behaviour of a Boom Clay sample extracted from the HADES URL at Mol (Belgium). In this particular example, the standard and new model lead to similar fitted Young's modulus. However, viscoelasticity leads to significantly improved predicted permeability values, especially for those stages where the confining pressure decreased.
- Similar results are obtained when validating against a specimen of the Callovo-Oxfordian claystone collected from the Meuse/Haute Marne URL (France). The proposed enhancement leads to better fitting in those cases where the elastic model is not appropriate and provides a very similar solution when the traditional model is

accurate enough. As observed for the Boom Clay sample, this improvement is especially significant for the permeability parameter.

- The consolidation experiments conducted on a sample recovered from the Upper Mercia Mudstone Group formation in the Larne Basin (Northern Ireland) are also better described with the proposed viscoelastic model rather than the standard Biot's model. Despite the high heterogeneity, better approximations of the Young's modulus and the permeability values are obtained if the medium is enhanced with a dashpot viscosity.

In all cases considered, this simple approach leads to an improved ability to predict the mechanical response of clay-based porous materials during loading and unloading. As such, incorporation of this visco-elastic component to deformation may result in improved predictions when assessing mechanical performance of natural and engineered barrier materials in geological applications such as the disposal of radioactive waste and the subsurface storage of CO_2.

Acknowledgements

The study was undertaken by staff of the Minerals and Waste Programme of the British Geological Survey (BGS) using the experimental facilities of the Transport Properties Research Laboratory (TPRL). This work was supported by the Engineering and Physical Sciences Research Council [grant number: EP/K036025/1]. Mercia Mudstone samples were collected with kind permission of the Carrickfergus salt mine. This paper is published with the permission of the Executive Director, British Geological Survey (NERC).

References

Armitage, P.J., Worden, R.H., Faulkner, D.R., Aplin, A.C., Butcher, A.R. and Espie, A.A. (2013). *Journal of the Geological Society*, 170, 119-132, doi: 10.1144/jgs2012-049.

Atkinson, J.H. and Bransby, P.L. (1978). The Mechanics of Soils: An Introduction to Critical State Soil Mechanics. McGraw-Hill, New York.

Bardet, J.P. (1992). A viscoelastic model for the dynamic behavior of saturated poroelastic soils, *Journal of Applied Mechanics*, 59(1) 128–135. doi: 10.1115/1.2899417.

Barnichon, J.D. and Volckaert G. (2003). Observations and predictions of hydromechanical coupling effects in the Boom clay, Mol Underground Research Laboratory, Belgium. *Hydrogeology Journal*, 11(1), 193-202. doi: 10.1007/s10040-002-0240-6.

Bésuelle, P., Viggiani, G., Desrues, J., Coll, C. and Charrier, P. (2013). A Laboratory Experimental Study of the Hydromechanical Behavior of Boom Clay. *Rock Mechanics and Rock Engineering*, 47(1), 143–155. doi: 10.1007/s00603-013-0421-8.

Biot, M.A. (1941). General Theory of Three-Dimensional Consolidation. *Journal of Applied Physics*, 12(2), 155-164. doi: http://dx.doi.org/10.1063/1.1712886.

Bishop, A.W. and Lovebury, H.T. (1969). Creep characteristics of two disturbed clays. *Proceedings 7th International Conference Soil Mechanics and Foundation Engineering*, Mexico.

Bjerrum, L. (1967). Progressive failure in slopes of overconsolidated clay and clay shales, *Journal of the Soil Mechanics and Foundation Division*, American Society Of Civil Engineers, 93, No. SM5, 1-49.

Fowler, A.C. and Noon, C.G. (1999). Mathematical models of compaction, consolidation and regional groundwater flow. *Geophysical Journal International*, 136(1), 251-260. doi: 10.1046/j.1365-246X.1999.00717.x.

Hamiel, Y., Lyakhovsky, V. and Agnon, A. (2004) Coupled evolution of damage and porosity in poroelastic media: Theory and applications to deformation of porous rocks. *Geophysical Journal International*, 156(3), 701-713. doi: 10.1111/j.1365-246X.2004.02172.x.

Harrington, J.F., Cuss, R.J. and Talandier, J. (2017). Gas transport properties through intact and fractured Callovo-Oxfordian mudstones. From: Rutter, E. H., Mecklenburgh, J. & Taylor, K. G. (eds) Geomechanical and Petrophysical Properties of Mudrocks. Geological Society, London, Special Publications, 454, https://doi.org/10.1144/SP454.7.

Harrington, J.F. and Tamayo-Mas, E. (2016). Hydraulic properties of the Callovo Oxfordian mudrock: sensitivity to changes in stress. Commercial-in-confidence report CR/17/007.

Harrington, J.F., Graham, C.C, Tamayo-Mas, E. and Parkes, D. (2018). Stress controls on transport properties of the Mercia Mudstone Group: importance for hydrocarbon depletion and CO2 injection. Marine and Petroleum Geology, 93, 391-408. doi: 10.1016/j.marpetgeo.2018.02.009.

Hobbs, P.R.N., Hallam, J.R., Forster, A., Entwisle, D.C., Jones, L.D., Cripps, A.C., Northmore, K.J., Self, S.J., and Meakin, J.L. (2002). Engineering geology of British rocks and soils – Mudstones of the Mercia Mudstone Group. *British Geological Survey Research Report,* RR/01/02.

Horseman, S.T., Winter, M.G. and Enwistle, D.C. (1987). Geotechnical characterization of Boom clay in relation to the disposal of radioactive waste (No. EUR--10987). Commission of the European Communities.

Horseman, S.T., Harrington, J.F., Birchall, D.J., Noy, D.J., Cuss, R.J. (2005). Consolidation and rebound properties of Opalinus Clay: a long-term, fully drained test. *British Geological Survey*, 72pp. (CR/05/128N)

Horseman, S.T. and Harrington, J.F (1996). Evidence for Thresholds, Pathways and Intermittent Flow in Argillaceous Rocks, Nuclear Energy Agency Workshop, Fluid Flow Through Faults and Fractures in Argillaceous Media, Berne, June 10–12.

Manoharan, N. and Dasgupta, S.P. (1995). Consolidation analysis of elasto-plastic soil. *Computers & Structures*, 54(6), 1005-1021. doi: 10.1016/0045-7949(94)00403-P.

Novello, E.N. (1988) Geomechanics and the critical state. Ph.D. Dissertation, Monash University, Melbourne, Australia.

Oka, F., Adachi, T. and Okano, Y. (1986). Two-dimensional consolidation analysis using an elasto-viscoplastic constitutive equation. International Journal for Numerical and Analytical Methods in Geomechanics, 10(1), 1-16. doi: 10.1002/nag.1610100102.

Scott, C. R. (1980). An Introduction to Soil Mechanics and Foundations. 3rd Edition. Applied Science Publishers LTD.

Skempton, A.W. (1970). The consolidation of clays by gravitational compaction. *Journal of the Geological Society*, 125, 373-441. doi: 10.1144/gsjgs.

Terzaghi, K. (1925). Erdbaumechanik auf bodenphysikalischer grundlage, Deuticke, Leipzig.

Wileveau, Y. and Bernier, F. (2008). Similarities in the hydromechanical response of Callovo-Oxfordian clay and Boom Clay during gallery excavation. *Physics and Chemistry of the Earth, Parts A/B/C*, 33(1), S343– S349. doi: http://dx.doi.org/10.1016/j.pce.2008.10.033.